Pre- and post-failure dynamics of landslides in the Northern Apennines revealed by space-borne synthetic aperture radar interferometry (InSAR)

Published Version:
Squarzoni G., Bayer B., Franceschini S., Simoni A. (2020). Pre- and post-failure dynamics of landslides in the Northern Apennines revealed by space-borne synthetic aperture radar interferometry (InSAR). GEOMORPHOLOGY, 369, 1-12 [10.1016/j.geomorph.2020.107353].

Availability:
This version is available at: https://hdl.handle.net/11585/787218 since: 2021-01-07

Published:
DOI: http://doi.org/10.1016/j.geomorph.2020.107353

Pre and post failure dynamics of landslides in the Northern Apennines revealed by space-borne synthetic aperture radar interferometry (InSAR)

Squarzoni, Gabriela[a], Bayer, Benedikt[b], Franceschini, Silvia[b], Simoni, Alessandro[a,*]

[a] *Via Zamboni 67, Bologna, University of Bologna*
[b] *Viale Fanin 48, Bologna, Fragile srl*

Abstract

Landslides are common landscape features in the Northern Apennine mountain chain and cause frequent damages to human structures and infrastructure. Most landslides in the area can be classified as earthflows, where the clay-shales form the substrate, whereas complex landslides with flow and sliding components are common on the slopes where fine-grained turbidites form the substrate. Most of these landslides move periodically with contained velocities and, only after particular rainfall events, some of them accelerate abruptly. Space-borne synthetic aperture radar interferometry (InSAR) provides a particularly convenient way for studying the periods before and after failures. In this paper, we present InSAR-results derived from the Sentinel 1 satellite constellation for two landslide cases in the Northern Apennines. The first case is a complex landslide that is hosted on a pelitic flysch formation, whereas the second case is an earthflow located in chaotic clay shales. Both cases failed catastrophically and threatened or damaged important infrastructures. In the case of the complex landslide, we report spatially variations of the deformation field between repeated periods of acceleration. The data illustrate that the deformation initiated in the upper part of the slope and expanded over the whole landslide body afterward. In the case of the earthflow, we describe spatial and temporal kinematics during the period before a catastrophic failure in March 2018. We discuss the temporal deformation signal together with rainfall and snowmelt data from a nearby meteorological station. Deformation and precipitation data highlight that high total precipitation can be considered the trigger of the failure.

Keywords: `InSAR`, `landslides`, `earthflows`, `failure`, `rainfall`, `snowmelt`

*Corresponding author
Email address: `alessandro.simoni@unibo.it` (Simoni, Alessandro)
URL: `www.fragilesrl.it` (Bayer, Benedikt), `www.fragilesrl.it` (Franceschini, Silvia)

1. Introduction

Landslides are common morphological features throughout the whole Northern Apennines chain. Most slope deformations occur on old landslide materials that failed in the past (Bertolini et al., 2004). In many cases, the reactivation of old deposits causes the regression of the main scarp and the physical degradation of the material which may move downwards as an earthflow. In other cases, the reactivation is more complex and different types of landslides can occur (Bertolini and Pellegrini, 2001). Because the typical velocity of most of these landslides can span from centimeters per year to meters per hour, depending on the stage of life (Cruden and Varnes, 1996), it becomes important to properly monitor the displacements of the involved masses to assess the possibility of sudden accelerations.

A powerful technique for monitoring the displacements of large areas is the synthetic aperture radar interferometry (InSAR) that provides the possibility to measure the deformations of the landslide deposits during the slow-motion stage (i.e., before the rapid acceleration). InSAR was applied in a landslide-prone area in the mid-1990s (Fruneau et al., 1996), but only in the 2000s it became a well-known technique for landslide monitoring. The development of multi-temporal methods (e.g. Ferretti et al., 2001; Berardino et al., 2002; Hooper et al., 2004; Hooper, 2008) helped in many cases to obtain useful InSAR derived information on the displacement of landslides. Those techniques have been developed to overcome some of the limitations that conventional two-pass interferometry had shown until that time (Colesanti and Wasowski, 2006; Wasowski and Bovenga, 2014). Since then, different InSAR techniques have been used to retrieve spatial and temporal deformations of landslide-prone slopes in soft rocks (Colesanti et al., 2003; Hilley et al., 2004; Wasowski and Bovenga, 2014; Handwerger et al., 2015; Bayer et al., 2017, 2018).

The two most common multi-temporal techniques are the Persistent Scatterer interferometry (PS-InSAR, Ferretti et al., 2001) and Small Baseline techniques (SBAS, Berardino et al., 2002, Schmidt and Bürgmann, 2003): the former is based on the stable SAR response of specific targets (i.e. stable scatters), computed by using single-master interferograms series; the latter is often optimized to derive spatially distributed information of multi-master interferograms series. Other techniques combine the advantages of both techniques (Hooper, 2008).

PS-InSAR and small baseline techniques are widely used for landslide studies (Bianchini et al., 2013; Tofani et al., 2013; Wasowski and Bovenga, 2014; Raspini et al., 2019), but in mountainous areas the quality of measurements is often affected by decorrelation from the environmental setting and in particular the presence of snow during the winter months and vegetation in the rest of the year. In such contexts, stable scatters detection is constrained to human structures which are characterized by high coherence values. Thus, decorrelation issues are still challenging in scarce-urbanized areas.

In the past, only L-band data delivered spatially quasi-continuous data in settings similar to the northern Apennines. The few reported examples, however, resolve mainly on the seasonal kinematics of slow-moving landslides in California (Roering et al., 2009; Handwerger et al., 2013). The launch of the new Sentinel 1 satellite constellation, which is characterized by a high acquisition frequency of up to six days, is suited to reduce decorrelation in the derived interferograms (Intrieri et al., 2018; Carlà et al., 2018) and permits to obtain promising results with higher temporal resolution (Handwerger et al., 2019).

In this paper, we investigate the response of two landslides using InSAR analysis. Because the landslides are located in rural areas with scarce urbanization, we use standard InSAR and explore its potential in capturing the changeable rates of displacement and spatial patterns of deformation. The two landslides were selected because they experienced catastrophic failures (here defined as stage A of the morphological classification reported in Picarelli et al. (2005); failure in the following), during the time span of our investigation. These circumstances offer the possibility to explore standard InSAR potential to detect pre- and post-failure deformations and document its evolution through time. Though such documentation has been previously reported for instrumented landslides (e.g., Scoppettuolo et al., 2020), the possibility to use InSAR implies the advantages intrinsic to remote sensing techniques that open to applications that include areal surveillance and early detection.

We show that the technique is capable of producing spatially quasi-continuous maps of deformation, also in areas that are characterized by the absence of good quality reflectors. Our data indicate that, in both cases, the failure was preceded by detectable deformation. InSAR results document the pre-failure and post-failure stages of the movement in terms of its spatial pattern and temporal evolution. In one of the two cases, we could derive actual displacement time-series that were compared to the precipitation regime to identify the triggering condition.

2. Geological and geographical background

The northern Apennine mountain chain is a pile of thrust and nappe units, transported towards the Padan-Adriatic-Ionian-Hyblean foreland starting from Late Oligocene times. In the Northern Apennines, the most common lithologies are chaotic clay shales and flysch deposits (Royden et al., 1987; Castellarin, 1992; Patacca et al., 1993; Marroni and Treves, 1998).

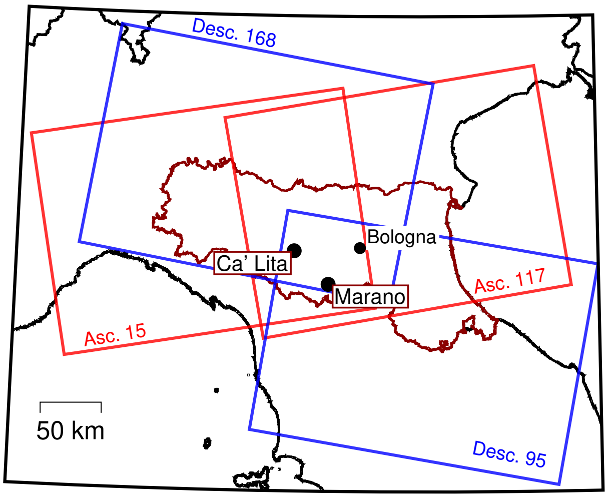

Figure 1: Location of the investigated landslides and setting of the satellite Tracks over the area.The region boundaries are highlighted by the dark red line and the landslides sites are labeled. The red boxes represent ascending Tracks and the blue boxes represent the descending Tracks.

The northern Apennines are affected by a high density of landslides and Bertolini and Pellegrini (2001) reported more than 32,000 landslides over the region of Emilia Romagna. In the classification scheme of Cruden and Varnes (1996), most of them can be described as complex landslides, associating roto-transitional slides with earthflows. Typical velocities are millimeters to centimeters per year during the dormant phase (which may last years to hundreds of years) and may increase up to meters per hour during the failure. The failure stages typically occur after periods of large amount of rainfall. The average annual rainfall at elevations similar to those of the two case studies is around 1200 mm, but the pluviometric regime is not uniform and 75% of the total rainfall occurs in two rainfall seasons, one of which occurs during fall and one during spring (Bertolini and Pellegrini, 2001; Berti and Simoni, 2012; Berti et al., 2012). The investigated cases are located in the Northern Apennines of Italy and both of them are covered by four Sentinel satellite orbits, two of which imaged the area in ascending geometry, whereas the other two swaths cover in descending geometry (Fig 1). The landslides reached the failure in the period covered by Sentinel 1 flights. Marano reactivated in March 2018 and Ca Lita in March 2016 and November 2017.

2.1. The Ca Lita landslide

The Ca Lita landslide (Fig. 1, 2 a) developed on a hillslope composed of flysch and clay-shales belonging to the Ligurian Units (Papani et al., 2002). It is located between 230 and 640 m a.s.l. in the Reggio Emilia province (Italy); the total length is 2.7 km, with a mean slope angle of 15 degrees and a total estimated volume of 40 Mm^3. The landslide can be classified as a reactivated complex landslide (Cruden and Varnes, 1996), in which a rotational rock slide in the head zones (in the Monghidoro Flysch Formation) evolves into an earthflow in the lower main body (in the Rio Cargnone Clayshales). It reactivated several times in the last century (Borgatti et al., 2006; Corsini et al., 2006; Cervi et al., 2012).

One catastrophic failure occurred in early spring 2004 after an intense rainy and snowy period. During this reactivation, it reached peak velocities of about 10 m per day at the toe and only of few decimeters per day in the upper part (Borgatti et al., 2006; Corsini et al., 2006). After the reactivation, mitigation structures such as drainage systems and retaining walls, were built to stabilize the landslide. Since then, no further deep-seated movements have occurred (Cervi et al., 2012) until March 14th, 2016. During this reactivation, the flysch rocks belonging to the upper part failed and deformed in a roto-translational movement and caused the failure of a retaining wall (Fig. 2 b) and the mobilization of the landslide deposit in the lower part as a flow-like movement (Fig. 2 c). The photos show that the deformation varied from several meters in the upper part up to hundreds of meters in the lower part. The landslide mass slowed down towards the end of March 2016.

In the middle of November 2017, it accelerated again: the upper earthflow deposits partially reactivated and moved downslope. The first movements occurred in correspondence in the upper part of the earthflow deposit with estimated displacements of several meters. The intensity of the displacements gradually decreased in the lower portion. The velocity of the earthflow never reached a value of zero because on February 20th, 2018 it was affected by another small acceleration and in March 2018 changing geomorphological features like trenches, exposed material, and surface water ponds demonstrated that it kept moving (Servizio Geologico Sismico e dei Suoli della Regione

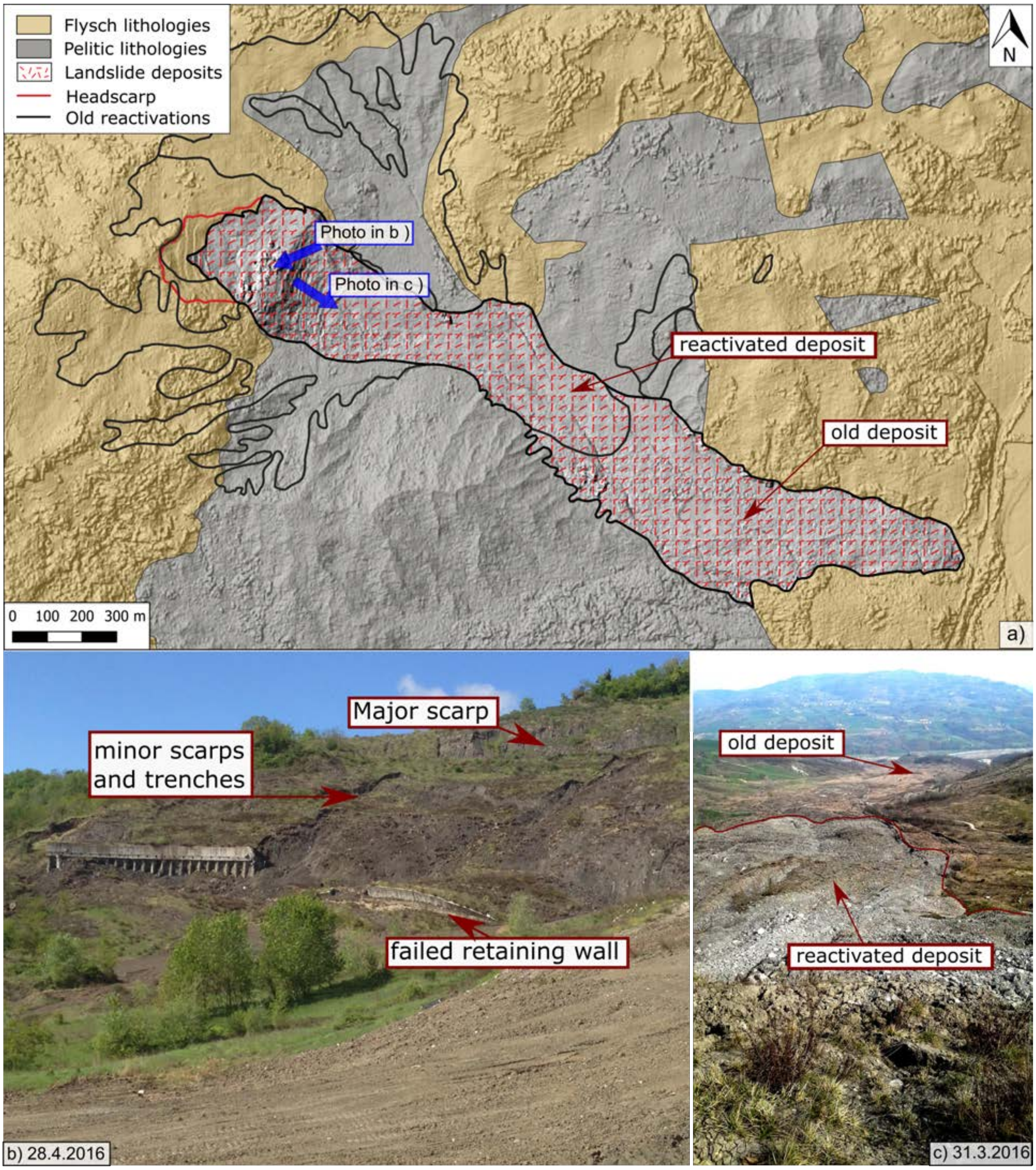

Figure 2: a) Map of the Ca Lita landslide with positions of the photos that were taken after the reactivation during March 2016. They show b) the rotational sliding in the upper part that caused the failure of the mitigation measurements (photo courtesy of Al Handwerger) and c) the flow like propagation in the lower part of the slope.

Emilia-Romagna, 2019).

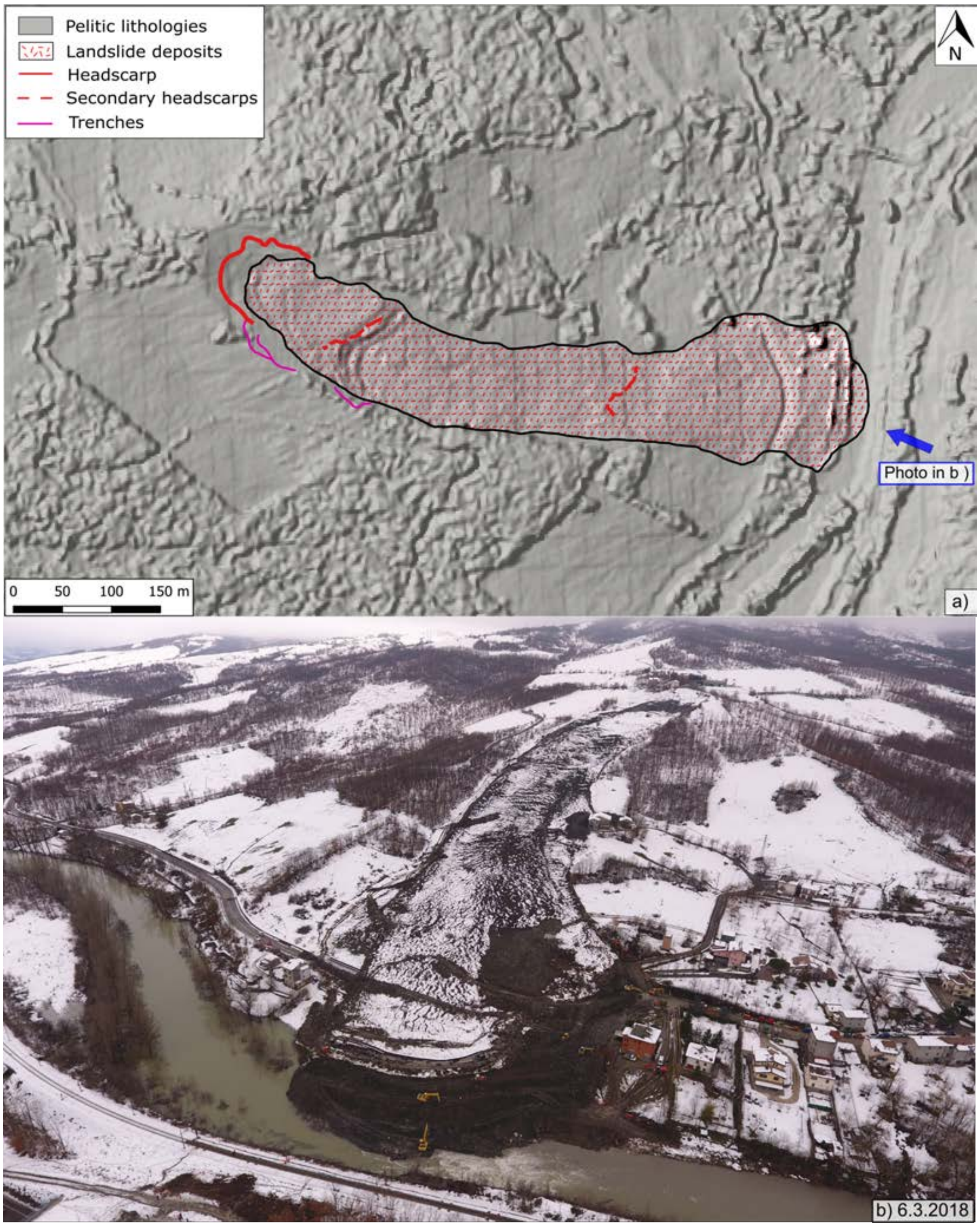

Figure 3: a) Map of the Marano earthflow with the deposits and the main morphological features related to the last reactivation being highlighted. b) Photo taken by a drone on the 6th of March 2018 (photo courtesy of Davide Marchioni).

2.2. *The Marano earthflow*

The Marano landslide (Fig. 1, 3) is located in the Bologna province (Italy) between 260 and 400 m a.s.l.; it is 700 m long and 100 m large for an estimated total volume of about 0.5 Mm^3. The landslide is a reactivated earthflow (Cruden and Varnes, 1996) that involve clay-shale lithologies belonging to the Palombini Shale Formation (Panini et al., 2002). During the last century, it reactivated twice: February 1996 and March 2018.

The 1996 event occurred after a period of intense rainfalls and snowfalls. The first motion had been recorded on February 1st in the upper portion of the slope and rapidly propagated downslope; after 6 days of rapid movement, it slowed down. The slope failure intersected different infrastructures like roads, methane pipelines, phone and electricity lines (Servizio Geologico Sismico e dei Suoli della Regione Emilia-Romagna, 2019). In the following period, mitigation strategies were adopted including drainage systems in the earthflow deposits and gabions in the lower part of the landslide to preserve the road below. For more than 20 years no signs of deformation were observed on the rebuilt road, in the gabions or the earthflow area. On March 1st, 2018 the landslide accelerated, however, after a period of snowmelt and rainfall. The mitigation structures were destroyed and the deposits reached the Reno river which is well visible in Fig 3 b. The Marano landslide moved with velocities of several meters per day for at least ten days, then decelerated. In the following days, employees worked at the earthflow toe and removed a large amount of material that was occluding the Reno river and also threatening the railways on the opposite bank.

3. Materials and Methods

3.1. *Synthetic aperture radar interferometry (InSAR): limitations and techniques*

Space-borne synthetic aperture radar interferometry (InSAR) is a remote sensing technique that exploits the phase difference between two radar images that were acquired over a given track of the earth surface by a satellite. Part of the phase difference is caused by the deformation of the targets inside a pixel with respect to the sensor (Massonnet and Feigl, 1998; Rosen et al., 2000; Bürgmann et al., 2000). It has been widely used for different applications in earth-sciences including earthquakes (Fialko et al., 2005), land subsidence and uplift of aquifers (Schmidt and Bürgmann, 2003; Chaussard et al., 2014) or because of glacial processes (Auriac et al., 2013, 2014), volcanic deformation (Hooper et al., 2007), but also for landsliding (Bianchini et al., 2013; Handwerger et al., 2013; Raspini et al., 2019). InSAR, however, presents three major limitations which are related to each other.

1. **Phase ambiguity**: The differential phase of an interferogram is ambiguous because it is measured as a fraction of the wavelength and a deformation field will be mapped in the range between -π and π radians. At this stage, the interferometric phase is typically called wrapped phase and in deforming areas a spatial pattern that is called interferometric fringes can often be observed (Massonnet and Feigl, 1998, e.g.). The transgression from one end of the spectrum to the other is occasionally also referred to as phase-jump. Resolving this phase-ambiguity to obtain absolute values requires a process that is called phase unwrapping and in the past different techniques were proposed to address this problem (e.g. Chen and Zebker, 2001; Hooper and Zebker, 2007). If the deformation field develops over a small area, an under-sampling of the phase-jump may occur that will result in an unwrapping error.
2. **Decorrelation:** One major draw-back of InSAR, especially in rural areas, is signal loss that is also referred to as coherence loss or decorrelation of the interferogram (Zebker and Villasenor, 1992). It occurs mainly when the surface between two acquisitions changes significantly (temporal decorrelation), for instance because the timespan of the interferogram is long, because deformation rates are high, because snow cover is present in one scene of the interferogram or because vegetation starts to grow. Decorrelation may also occur if the distance of the sensor between two acquisitions (known as perpendicular baseline) is large, which is called baseline decorrelation. In the presence of noise from decorrelation also the unwrapping will become more difficult and unwrapping errors will occur more frequently (Chen and Zebker, 2001).
3. **Contributions to the interferometric phase:** Even if the interferometric phase is coherent, it still contains contributions that can be regarded as noise if deformation is the main goal of the analysis. The main sources of the undesired signal are the differential phase from topography, atmosphere and orbital errors (Tarayre and Massonnet, 1996; Zebker et al., 1997; Fattahi and Amelung, 2015).

Since the 1990s numerous space-borne SAR missions with three different wavelengths have been active, ranging from short wavelength satellites with high spatial resolution of ca. 3 m (3 cm X-BAND, COSMO-Skymed, TerraSAR-X) over C-Band with variable spatial resolutions (5.6 cm, ERS, Envisat or Sentinel-1) to 23 cm L-Band sensors like JERS, ALOS PALSAR or ALOS PALSAR-2 (see for instance Wasowski and Bovenga, 2014 for an exhaustive list). Because the differential phase is measured as fraction of the satellite wavelength, short wavelength sensors are potentially more sensitive to small displacements compared to long wavelength sensors, whereas they will have more problems with decorrelation and unwrapping errors. Also, long wavelength InSAR datasets are known to maintain coherence well also in rural areas (e.g. Handwerger et al., 2013; Schlogel et al., 2015), because longer wavelength radar waves can penetrate superficial vegetation and even canopy (e.g. Prush and Lohman, 2014; Ni et al., 2014).

Different multitemporal techniques, like persistent scatterer interferometry (Ferretti et al., 2001; Hooper et al., 2004), evolutions of it (Ferretti et al., 2011), small baseline techniques (Berardino et al., 2002; Schmidt and Bürgmann, 2003) or hybrid approaches (Hooper, 2008), were developed to address the problems of decorrelation and estimate different error terms of the phase. They were frequently used in the past to infer spatiotemporal information of slope deformations both on the scale of single slopes (Wasowski and Bovenga, 2014), as well as on larger scales (Raspini et al., 2019). Near to the study area, small baseline techniques proved useful to assess tunneling induced deformation (Bayer et al., 2017), but also the relationship between seasonal creep of landslides from variations of precipitation (Bayer et al., 2018). All of the aforementioned works used techniques that focused on extracting highly coherent pixels mostly on human structures, like houses or exposed rock-outcrops. In the study area, however, most active landslides have a moderate vegetation cover, rarely have exposed landslide material and only slow-moving deep-seated landslides have human structures on them.

Similar geomorphological and geological conditions exist in Northern California, where only long-wavelength data from ALOS permitted to reveal relationships between earthflow deformation and the precipitation regime (Handwerger et al., 2013, 2015; Bennett et al., 2016), and in combination with offset tracking techniques also the slow down of earthflows because of extreme drought conditions. Most recently, however, Handwerger et al. (2019) have shown that also the C-band data acquired by Sentinel 1 can be successfully used to obtain high-quality interferograms on types of landslide similar to the ones described in this paper.

3.2. InSAR datasets and processing

We performed interferometric processing of synthetic aperture radar images acquired by Copernicus Sentinel 1 A/B satellites by using GMTSAR (Sandwell et al., 2011) and unwrapped the complex interferograms with the Statistical-Cost, Network-Flow Algorithm (SNAPHU; Chen and Zebker, 2001). The Sentinel images are C-band images (5.6 cm radar wavelength) acquired with a minimum interval of acquisition of six days (12 days for each satellite, with a six days interval between Sentinel 1A and Sentinel 1B). We studied the period between January 2015 and January 2019 by analyzing two descending orbits (south-moving satellites, looking west) and two ascending orbits (north-moving satellites, looking east) for a total of four datasets for each landslide: Track 168, Track 95, Track 15 and Track 117 (Fig. 1). We initially processed a total of 869 interferograms for the Marano landslide and 1419 interferograms for the Ca Lita landslide that were inspected visually and only interferograms with a clear phase signal were considered for further processing.

The topographic phase was calculated and subtracted (e.g. Massonnet and Feigl, 1998; Bürgmann et al., 2000) by using an external digital surface model (2x2 m DSM, provided by the Emilia Romagna Region Services). Because of the small perpendicular baselines of Sentinel 1, the residual DEM error is small compared to the signal from landslide motion and a correction scheme, like the one proposed in (Fattahi and Amelung, 2015), proved not necessary. The large scale atmospheric noise has been reduced by high pass filtering the interferograms and by selecting a stable reference area close to the deforming region: we chose geomorphological (e.g. ridges) or anthropic features (e.g. stable buildings) located near the landslides. Moreover, Gaussian and Goldstein filters (Goldstein and Werner, 1998) have been applied after the interferograms formation to reduce the noises and enhance the deformation signal.

Despite the high acquisition frequency of Sentinel-1, unwrapping problems continued to arise on the landslides during periods of high rates of displacement. Handwerger et al. (2015, 2019) proposed a strategy to forward model the deformation to solve these unwrapping problems. We adopted a similar approach that consisted in forming a deformation model by calculating the mean rate of displacement from all interferograms without unwrapping errors. Then we used SNAPHU's option that offers the possibility to subtract a deformation model before unwrapping adding it back afterwards.

This approach helped to solve phase-jumps over the Marano landslide, whereas at the Ca Lita landslide it only helped in few cases. This is probably because the Marano earthflow deformed in a coherent slab, whereas the Ca Lita landslide has complex sliding features in the upper part with high relative displacements and flow like deformation in the lower part with high absolute displacements.

After this manual and iterative process of inspecting and improving interferograms, only those without severe phase unwrapping problems were used to produce stacks of interferograms that contain mean velocities and, in case of the Marano landslide, velocity time series.

We describe our results in terms of line-of-sight (LOS) displacement and velocity. Downslope projection (Hilley et al., 2004) was not used to avoid the introduction of uncertainties deriving from DEM-derived average slope and direction. In the case of our landslides, because of west-dipping, moderately steep (10 to 20) slopes, positive and negative LOS displacements indicate downslope movement for the ascending and descending orbit respectively. The downslope movement of earthflows is dominated by translation though vertical components can act at the toe or in the source area (Picarelli et al., 2005).

4. Results

4.1. Spatial deformation patterns on the Ca Lita landslide

The kinematics of the Ca Lita earthflow are characterized by repeated variations of the rates of displacement with values that exceed the detection limits of spaceborne radar interferometry. Although at times it moves too fast to derive displacement or velocity time-series, a clear spatial deformation pattern, roughly corresponding to the main landslide deposit, can be detected in a large number of interferograms. Stacking series of interferograms, corresponding to a given time-interval, increases the signal-to-noise ratio and highlights deforming features. The analysis and comparison of successive interferometric stacks allow obtaining spatial and temporal information about the landslide during phases of slow rates of displacement. During the failure stages, decorrelation and unwrapping problems from fast-displacement can not be resolved, which is why the mean velocities computed from the stacking process are locally underestimated. The spatial deformation signal, however, is clear and can be used to document the evolution of the landslide movement just near the activation stages.

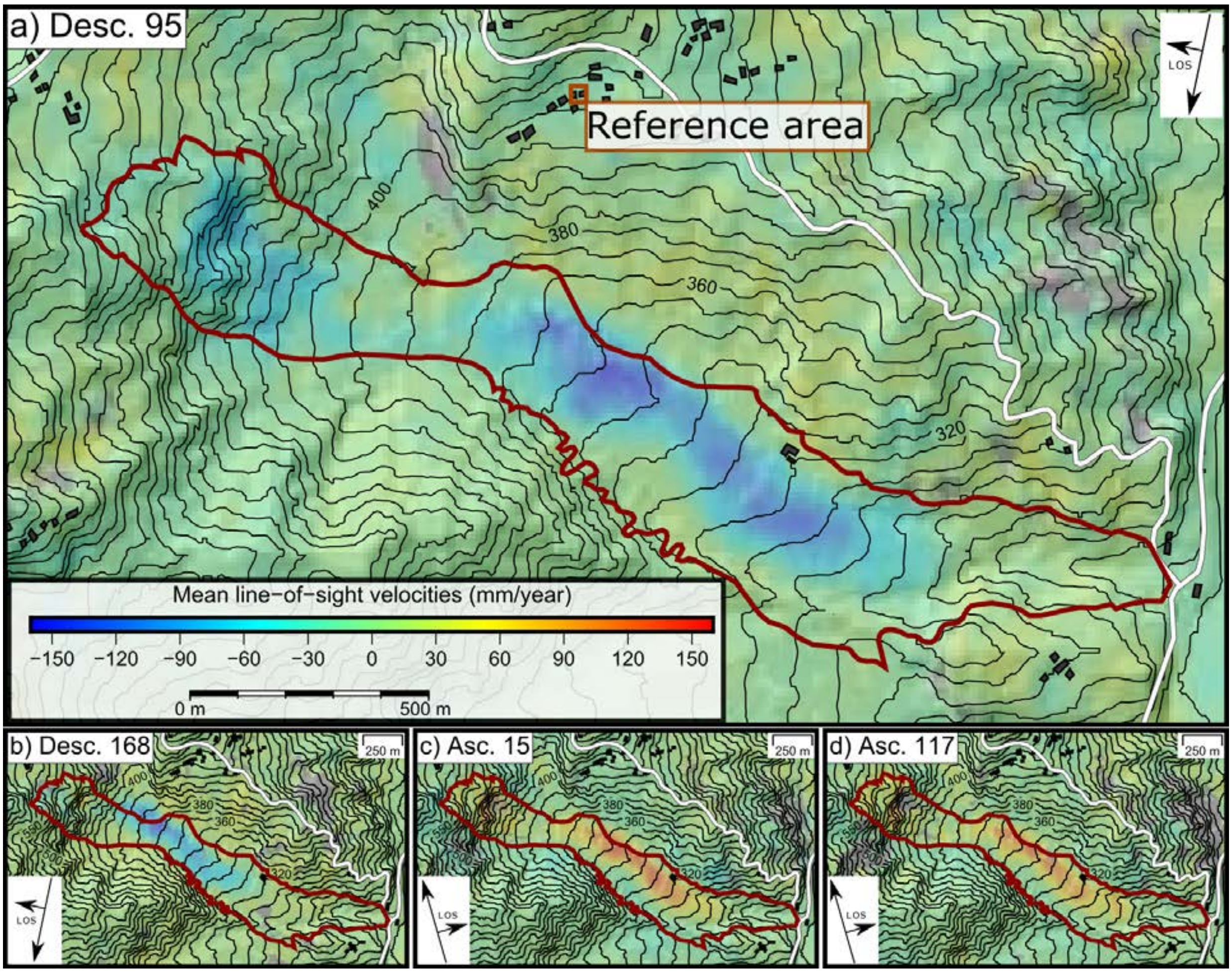

Figure 4: Ca Lita stacks of the entire interferograms series, concerning the period between January 2015 and January 2019: the numbers of the satellite Tracks are labeled at the top right of each image and the orbit directions are indicated at bottom right. Positive (red) values indicate motion away from the satellite along the line-of-sight and negative (blue) values indicate motion toward satellite along the line-of-sight. The numbers of interferograms that have been used to compute the stacks are: a) 286, b) 352, c) 372, d) 409. All the pixels averaging a value of coherence lower than 0.2 have been masked out in the figure and display grey color.

The stack of all manually-selected interferograms (from January 2015 to January 2019) highlights the long-shaped morphology of the Ca Lita earthflow, that corresponds to the landslide deposit of the prior reactivation (Borgatti et al., 2006; Corsini et al., 2006; Servizio Geologico Sismico e dei Suoli della Regione Emilia-Romagna, 2019). The interferometric signal is particularly clear in the descending orbit 95 (Fig.4 a), whose stack indicates a range decrease and, hence, a movement towards the satellite. This observation is confirmed by descending orbit 168 (Fig.4 b).

Whereas the ascending orbits (117 and Fig.4 c and d) record range increases and, hence, movements away from the satellite. In all cases, we used a mean coherence threshold of 0.25 to mask out areas affected by low coherence. Because of the selection procedure of the interferograms, coherence is, however, higher than 0.25 in most interferograms, which is why very few areas are masked out.

The difference between the ascending and the descending geometries should be interpreted as a real deformation field that is oriented approximately down-slope. Maximum rates of displacement are detected in the central part of the slope, where the type of movement transitions from sliding to flowing. The landslide toe is relatively stable (no interaction with the national road was reported) as well as the area above the crown, where houses are located, exhibit no deformation.

To document the temporal evolution of the Ca Lita landslide, we combined interferograms in bimonthly stacks. We found that such frequency was suitable to resolve the different deformation phases of this landslide. Fig. 8 reports the results derived from the descending orbit 168. The failure of March 2016 is not clearly documented by radar interferometry because of persisting snow cover in the area, which impeded to form coherent interferograms during this period. After failure, the Ca Lita landslide exhibits enduring deformation: in the summer period the displacement signal that is oriented towards the satellite is less evident and is located mainly the central portion of the deposits (Fig.5 - a, b). In late fall of 2016 (Fig.5 b) and early 2017 (Fig.5 c) almost all the landslide deposit is actively deforming.

At the beginning of 2017, the range of displacements decreases and are mainly located in the central part of the slope where flow-like deformation is dominant and where the slope decreases (Fig.5 c). In the upper part, small range increases were registered by the interferograms that span this period. During the summer months, the slope was relatively stable with rates of LOS (Line-Of-Sight) displacement lower than 100 mm/month. During September-October 2017 deformation is intense ($>$ 150 mm/year) and localized in the upper part of the landslide (Fig.5 d) where the slope is relatively steep and sliding transitions into a flow-like type of movement. Following the failure of November 2017, the whole landslide body, except for the toe, continued to move (Fig.5 e) though rates of displacement appear generally lower. In the following period, the landslide activity is clearly visible in the interferograms throughout the duration of our analysis. The LOS velocities are locally sustained ($>$ 150 mm/year), especially during the rainy season e.g., Nov.-Dec. 2018 stack in Fig.5 f).

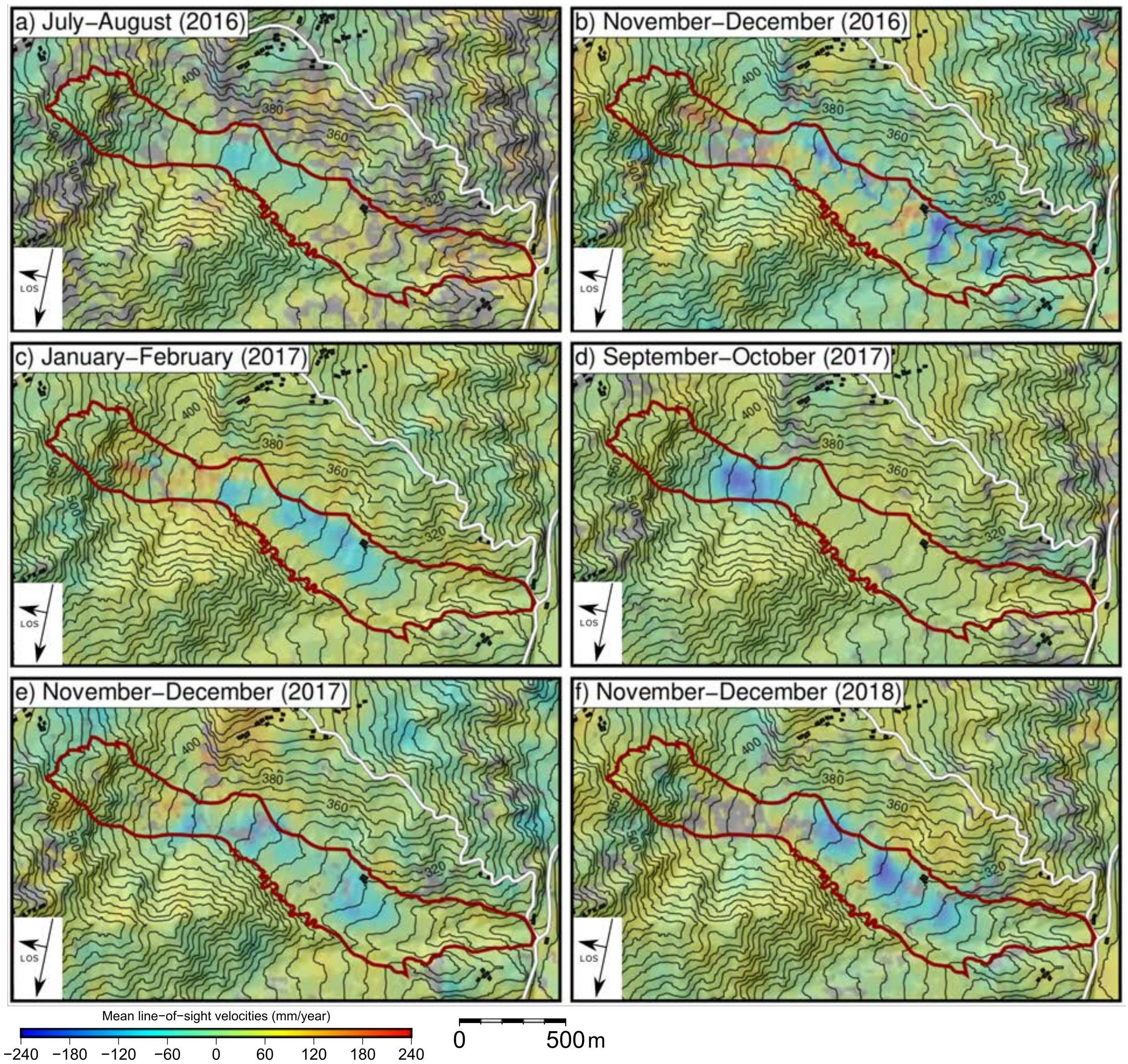

Figure 5: Two-months stacks for Track 168: a) July - August: 7 interferograms used for the stacking, b) November - December 2016: 10 interferograms used for the stacking, c) January - February 2017: 9 interferograms used for the stacking, d) September - October 2017: 8 interferograms used for the stacking, e) November - December 2017: 10 interferograms used for the stacking, f) November - December 2018: 10 interferograms used for the stacking. Three stages of movement can be observed: from a) to c) the deformation involves a very large portion of the deposits; in d) only the upper part in interested by displacements; from e) to f) the whole mass is involved again. Positive (red) values indicate motion away from the satellite along the line-of-sight and negative (blue) values indicate motion toward satellite along the line-of-sight. All the pixels averaging a value of coherence lower than 0.2 have been masked out in the figure and display grey color.

4.2. Pre-failure kinematics of the Marano earthflow

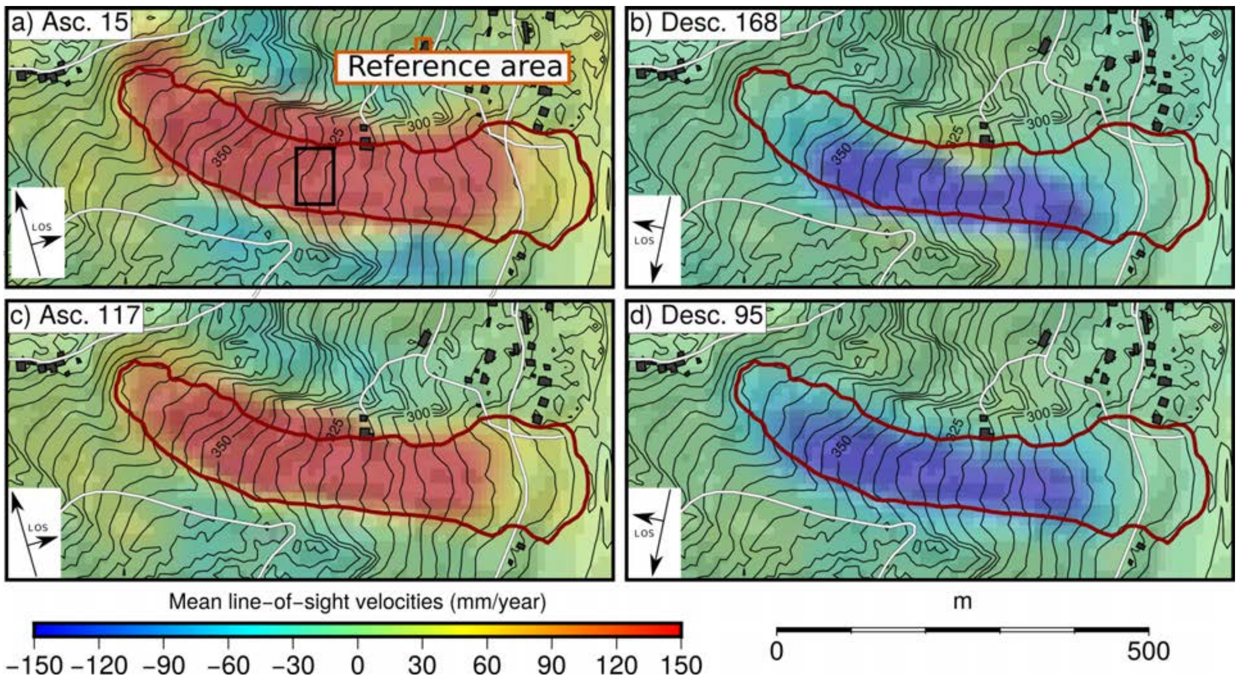

Figure 6: Marano stacks of the entire interferograms series, concerning the period between January 2015 and January 2019 derive from a) the ascending orbit 15 using 161 interferograms (the black box indicates the pixels that were used for the timeseries in figure 7, b) the descending orbit 168 using 218 interferograms c) the ascending orbit 117 using 209 interferograms and d) the descending orbit 95 with 281 interferograms. Warm colours indicate a movement away from the satellite along the line-of-sight, whereas cold colours indicate a movement towards the satellite. All the pixels averaging a value of coherence lower than 0.2 have been masked out.

The Marano earthflow reactivated catastrophically on March 1st, 2018 after 22 years of dormancy. The vast majority of selected interferograms (January 2015 to January 2019) detect active deformation along the slope. The apparently dormant landslide has been affected by detectable deformation for at least two years before the catastrophic failure occurred. The stack of all manually-selected interferograms shows an extremely clear signal detected by all available orbits (Fig. 6). The reference area was chosen with respect to the houses of the locality Marano and the ascending orbits show an almost identical spatial signal that indicates a range increase and, hence, a movement away from the satellite with more than 150 mm/year along the line-of-sight. The descending orbits, on the other hand, show a movement towards the satellite again with more than 150 mm/year along the line-of-sight. This difference can be interpreted as a gravitational deformation oriented along the downslope direction.

The deformation signal shown by the interferometric stacks is consistent for all orbits (Fig. 6) and indicates that surface displacements pervaded most of the landslide body with the exception of the toe. This latter propagated downslope tens of meters during the paroxysmal phase, partially damming the river and therefore being partially excavated. Our results, describe the pre- and post-failure phase and therefore do not capture effects of rapid deformation. Also, the displacement signal extending beyond the landslide perimeter in the ascending stacks (Fig. 6 a, 6 c) is compatible with slow deformation of small slope portions that were not involved in the actual mapped failure. Consider also that Sentinel spatial resolution is 20x5 m approximately and that noise-removal spatial filtering further diminish the effective ground resolution.

Compared to the Ca Lita landslide, the interferometric signal on the Marano earthflow is less noisy, because of lower rates of displacement , but also possibly because of the different kinematics. Whereas the Ca Lita landslide is dominated by roto-translational sliding in the upper part and flow-like deformation in the central and lower parts (Borgatti et al., 2006; Corsini et al., 2006), the Marano landslide appears to move as a relative coherent block along slope-parallel slip surface/s. Such response allowed us to successfully unwrap the Marano interferograms and extract velocity information for the period between the beginning of Sentinel acquisition and the failure (Fig.7, a).

The velocity series are obtained by simply dividing the displacement of each interferogram by the period between the two acquisitions that were used to form the interferogram. We used a local regression analysis to fit the data and detect associated trends (line in Fig.7, a). Before the launch of Sentinel 1B the frequency of velocity information is lower because only 12 and 24 days interferograms are available and few are selected because of coherence issues. This is why the trend before august 2016 is less defined. The most remarkable result is probably represented by the regression lines of the four independent datasets that depict similar and coherent trends. To interpret such trends, we compare them to the precipitation regime. The rainfall data have been provided by the Regional Agency for Prevention, Environment and Energy of Emilia-Romagna (Arpae) and the snowfalls data have been recorded at the Porretta station, respectively four and eight kilometers far from the earthflow and at a comparable elevation. For each hydrological year (starting in October) we calculated weekly rainfall values and cumulated precipitations (including both rainfall and snowmelt; Fig.7 b).

During 2016 (October 2015 - September 2016) the only peak in velocity was resolved during

March, following a period of intense rainfalls: about 300 mm of rain occurred in the previous 60 days. In the following year intense snowmelt and rainfall cause the rates of LOS displacement to exceed 100 mm/year in December 2016. In this case ascending datasets and descending dataset 95 capture the velocity peaking. During spring 2017 two peaks of high velocities were registered, the first one occurred in March, while the second in May. The peaks are well registered by the ascending dataset 117 and the descending dataset 95, whereas the other two orbits do retrieve high rates of displacement during spring but do not resolve two distinct peaks. Again, the velocity peaks follow two periods of precipitation with the first one being amplified by snowmelt.

During the dry summer of 2017, landslide velocities drop to almost null values along the line-of-sight, but with the onset of hydrological year 2017-2018, the landslide acceleration started almost synchronous with the first heavy precipitation of November 2017. The velocity continues to increase systematically until the failure of March 2018. Both the peak velocities as well as the slope of the velocity increases are higher compared to the previous years. Another difference between the period that precedes the failure and the years 2015-2017 is the snowmelt significantly contributes to an increase in the equivalent precipitation. The interferograms that directly precede or span the failure are heavily decorrelated all over the Reno catchment because of the presence of snow (3, b).

Once coherence is recovered (June 2018), the landslide is dormant and velocities are lower than they were during the years 2015-2017.

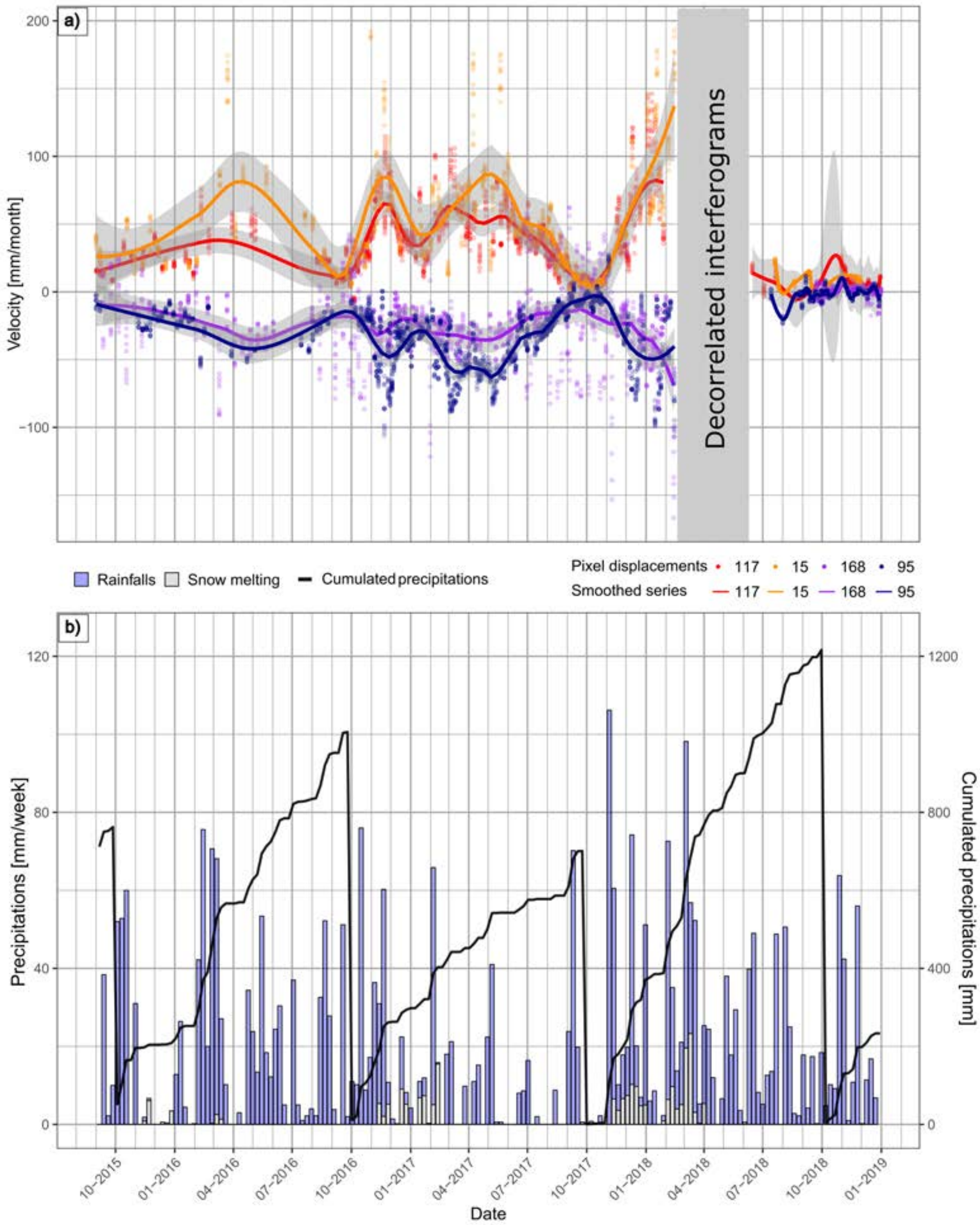

Figure 7: a) Velocity time series for each track at the Marano earthflow (positive values for ascending Tracks, negative values fo descending Tracks). The dot symbols represent the pixels belonging to the investigated area (see Fig.6); the lines are derived by applying a local regression smoothing using the implementation of the ggplot package that takes into account a neighbourhood of 20 % w.r.t. to complete series. The gray bands are the 95 percent confidence interval of the smoothing operation. The gray box highlights the time period in which interferograms are completely decorrelated either because of the presence of snow or because of high rates of displacement during the failure. b) Weekly data of rainfall and snowmelt (left y-axes) are plotted together with the cumulated precipitation that contains rainfall and snow-melt(right y-axes): the series has been set to zero at the beginning of each hydrological year.

5. Discussion and conclusions

Interferometric analysis has been successfully applied to two slow-moving landslides that were subject to generalized failures during the period of our investigations. Both landslides are characterized by the scarce presence of man-made structures or rock-outcrops that could represent stable scatterers in multi-temporal InSAR analysis. We used standard two-pass interferometry (Handwerger et al., 2013, 2019) to detect deformation signals useful to document the evolution of the landslides in the 2015-2019 interval. The InSAR data allow appreciating the spatial pattern of deformation at successive time intervals.

In the case of the Ca Lita landslide, the deformation maps evidence inhomogeneous deformation fields throughout the landslide deposit that can be used to interpret the kinematics of the phenomena. In fact, the pre-failure deformation at Ca Lita in 2017 was dominated by displacements localized in the upper part of the slope. This is consistent with the dynamics described for previous reactivation of this landslide (Borgatti et al., 2006; Corsini et al., 2006). Relatively fast displacements are detected in space but obtaining quantitative results is associated with larger uncertainties due to the presence of residual noise and unresolvable phase jumps. Though not numerically accurate during the most active phases of landslide movement, interferograms, and stacked interferograms contain useful information to: i) identify movement against surrounding stable slopes; ii) document the spatial evolution of the movement.

At Ca Lita, different types of movement can be encountered (i.e. sliding in the upper part and flow-like movement in the lower central and lower parts; Borgatti et al., 2006; Corsini et al., 2006), displacement rates were often sustained in between the two failure episodes (March 2016 - December 2017) and possibly associated to high spatial small-scale variability due to flow-like type of movement. Hence a velocity-time series similar to the one of the Marano case could not be produced. A conceptual sketch in Fig. 8 a) illustrates that deformation exceeding approximately 120 mm/month cause signals in interferograms that are not correct from a numerical point of view. This is because interferograms with higher displacement rates cause interferograms similar to those in Fig. 8 b) that show multiple phase jumps in the landslide area. The signal can be clearly attributed to deformation since coherence is high throughout the rest of the image. It is however impossible to correctly count the interferometric fringes that occur in this interferogram on the whole landslide body. There are also interferograms that are at the limit of decorrelation and have one or two phase jumps (Fig. 8 c) which can be unwrapped by forward modeling the deformation. Because the Ca Lita landslide has numerous open crevices and fissures along which high differential displacements occurred, it is possible that unwrapping undersampled some phase jumps.

From a geological point of view, the two analyzed landslide differ in several aspects. The bedrock at Ca Lita is composed of flysch rocks in the upper part and chaotic clay shales in the lower part of the slope, while the Marano earthflow is hosted only by chaotic clay shales. This difference in the bedrock material might contribute to the fact that at the Ca Lita landslide different kinematics coexist, while Marano is an earthflow like many others in the clay-shales rocks of the Reno Catchment where flow-like morphology is associated to dominant sliding (Simoni et al., 2013).

The Marano earthflow remained in a dormant state for 20 years before it reactivated in March 2018. No damages were reported along the national road crossing the landslide at the toe nor by the land owners upslope. However, InSAR data document active deformation for at least two years before the failure occurred. Marano earthflow interferograms indicate the coherent displacement of thelandslide deposits. Velocity variations are well documented by the velocity time series that we derive for each satellite track (Fig. 7). It has been possible to detect displacement rates ranging from virtually null values to more than 100 mm/month. The velocity time series show repeated and coherent velocity peaking that can be related to intense rainfalls and late summer velocity decline observed during 2016 and 2017. The main triggering factor is the precipitation regime during autumn 2017-spring 2018. The total amount of precipitation was significantly higher than average: 500 mm in the period between October 2017 and the failure (March 1st, 2018) most of them (100 mm) in the 30 days preceding the failure (Fig. 7). Snow melting contributed to significantly increase the equivalent precipitation during November and December 2017 and February 2018 when we calculate 80 mm of snow melting that is added to 340 mm of rain. Also, the hydrological year of 2017/2018 was preceded by an unusually dry summer which may have favored the formation of fissures and cracks on the landslide body increasing permeability and hence the infiltration of water (Malet et al., 2005).

From a technical point of view, results obtained on both cases show that standard InSAR can deliver almost continuous deformation maps on landslides of the Northern Apennines that are characterized by moderate vegetation and high displacement rates ranging from extremely slow to

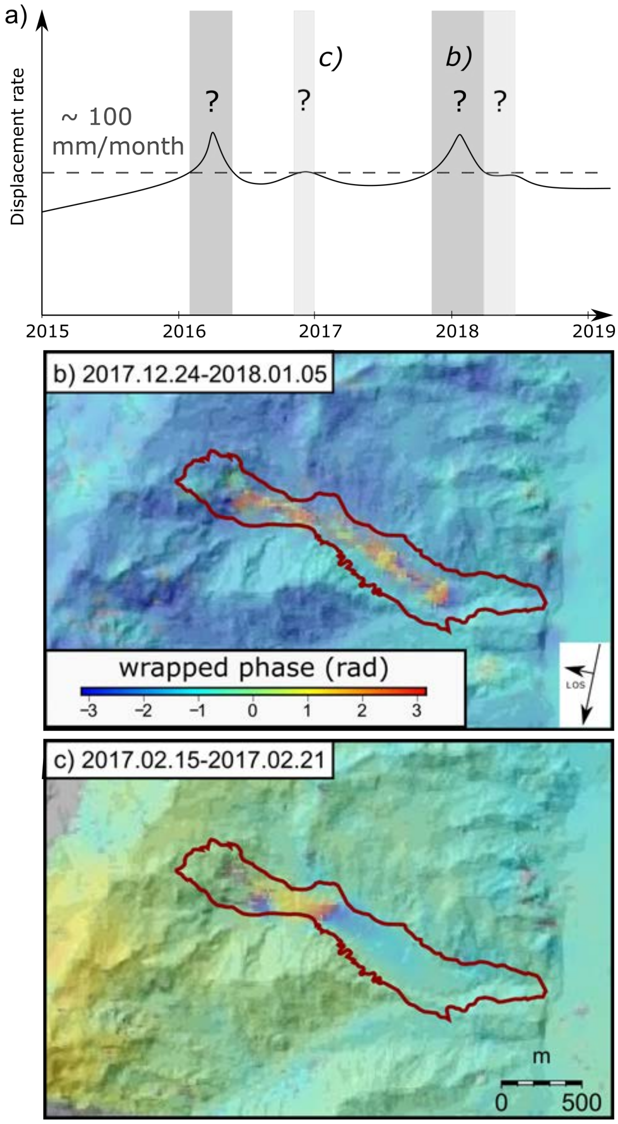

Figure 8: a) Conceptual sketch of the Ca Lita evolution. The dark gray boxes highlight periods in which several interferograms are decorrelated or display unwrapping problems because of fast displacement. The light gray boxes indicate periods in which displacement causes decorrelation in interferograms that span more than 12 days: the total number of decorrelated interferograms is slightly lower of that one referred to the dark gray boxes. The question marks in the gray boxes indicate the ambiguity of the the values for the rates of displacement if large decorrelation/unwrapping errors occur. In the other periods the velocity of the landslide is still often near to the upper limit and phase unwrapping may occurr. b) Example of wrapped interferogram with multiple phase jumps close to complete decorrelation ("fast-displacement decorrelation"). c) Example of wrapped interferogram (Track 168) with only one phase jump that can be solved in the unwrapping step. The labels on the top right indicate the temporal baselines of the two examples.

about 100 mm/month. When the velocities approach the upper limit and/or the landslide shows highly variable (pixel-scale) spatial deformation pattern, phase jumps cannot be further solved. At lower values, velocities can be considered reliable though inherent uncertainties associated to residual (topographic, atmospheric) noise remain. Despite the overall high quality of Sentinel 1 interferograms, we would like to remark the semi-quantitative significance of the displacement data obtained from standard InSAR analysis. Residual noise due to topography and atmosphere can, in fact, have a minor influence on the numerical displacement values that are obtained (Massonnet and Feigl, 1998; Bürgmann et al., 2000). Bigger accuracy issues are caused by localized pixel-scale shear zones resulting in phase jumps (Hu et al., 2019) and by displacement rates approaching the limits of the technique (Rosen et al., 2000; Bürgmann et al., 2000).

The present work shows that InSAR-derived deformation maps supply a lot of information about the spatial pattern and the temporal evolution of the landslides, also where stable reflectors are scarce or absent. In our cases, the generalized failures of slow-moving, apparently dormant earthflows were preceded by surface displacements that generated a clear interferometric signal. On the contrary, such deformations did not cause evident damages and went undetected on the ground. In a wider application perspective, we suggest that standard InSAR can provide qualitative monitoring that can be used to detect and follow the evolution of landslide displacements preceding (or following) a catastrophic failure. The high acquisition frequency of Sentinel 1 and the large spatial extension of SAR scenes open also new perspectives in using this approach for large scale analysis.

Acknowledgments

We would like to thank Al Handwerger and Davide Marchioni for photos providing. Rainfall data were obtained from the Dexter download system of ARPA Emilia Romagna (`http://www.smr.arpa.emr.it/dext3r/`). We thank the European Space Agency for supplying Sentinel data.

References

Auriac, A., Sigmundsson, F., Hooper, A., Spaans, K.H., Bjornsson, H., Palsson, F., Pinel, V., Feigl, K.L., 2014. Insar observations and models of crustal deformation due to a glacial surge in iceland. Geophysical Journal International 198, 1329–1341. doi:10.1093/gji/ggu205.

Auriac, A., Spaans, K.H., Sigmundsson, F., Hooper, A., Schmidt, P., Lund, B., 2013. Iceland rising: Solid earth response to ice retreat inferred from satellite radar interferometry and visocelastic modeling. Journal of Geophysical Research-solid Earth 118, 1331–1344. doi:10.1002/jgrb.50082.

Bayer, B., Simoni, A., Mulas, M., Corsini, A., Schmidt, D., 2018. Deformation responses of slow moving landslides to seasonal rainfall in the northern apennines, measured by insar. Geomorphology 308, 293–306.

Bayer, B., Simoni, A., Schmidt, D., Bertello, L., 2017. Using advanced insar techniques to monitor landslide deformations induced by tunneling in the northern apennines, italy. Engineering geology 226, 20–32.

Bennett, G.L., Roering, J.J., Mackey, B.H., Handwerger, A.L., Schmidt, D.A., Guillod, B.P., 2016. Historic drought puts the brakes on earthflows in northern california. Geophysical Research Letters 43, 5725–5731. doi:10.1002/2016GL068378.

Berardino, P., Fornaro, G., Lanari, R., Sansosti, E., 2002. A new algorithm for surface deformation monitoring based on small baseline differential sar interferograms. IEEE Transactions on Geoscience and Remote Sensing 40, 2375–2383.

Berti, M., Martina, M., Franceschini, S., Pignone, S., Simoni, A., Pizziolo, M., 2012. Probabilistic rainfall thresholds for landslide occurrence using a bayesian approach. Journal of Geophysical Research: Earth Surface 117.

Berti, M., Simoni, A., 2012. Observation and analysis of near-surface pore-pressure measurements in clay-shales slopes. Hydrological Processes 26, 2187–2205.

Bertolini, G., Casagli, N., Ermini, L., Malaguti, C., 2004. Radiocarbon data on lateglacial and holocene landslides in the northern apennines. Natural Hazards 31, 645–662.

Bertolini, G., Pellegrini, M., 2001. The landslides of the emilia apennines (northern italy) with reference to those which resumed activity in the 1994–1999 period and required civil protection interventions. Quad Geol Appl 8, 27–74.

Bianchini, S., Herrera, G., Mateos, R.M., Notti, D., Garcia, I., Mora, O., Moretti, S., 2013. Landslide activity maps generation by means of persistent scatterer interferometry. Remote Sensing 5, 6198–6222. doi:10.3390/rs5126198.

Borgatti, L., Corsini, A., Barbieri, M., Sartini, G., Truffelli, G., Caputo, G., Puglisi, C., 2006. Large reactivated landslides in weak rock masses: a case study from the northern apennines (italy). Landslides 3, 115.

Bürgmann, R., Rosen, P.A., Fielding, E.J., 2000. Synthetic aperture radar interferometry to measure earths surface topography and its deformation. Annual review of earth and planetary sciences 28, 169–209.

Carlà, T., Farina, P., Intrieri, E., Ketizmen, H., Casagli, N., 2018. Integration of ground-based radar and satellite insar data for the analysis of an unexpected slope failure in an open-pit mine. Engineering Geology 235, 39–52.

Castellarin, A., 1992. Strutturazione eo-e mesoalpina dell'appennino settentrionale attorno al" nodo ligure". Studi Geologici Camerti 1992/2, 99–108.

Cervi, F., Ronchetti, F., Martinelli, G., Bogaard, T.A., Corsini, A., 2012. Origin and assessment of deep groundwater inflow in the ca' lita landslide using hydrochemistry and in situ monitoring. Hydrology and Earth System Sciences 16, 4205–4221. URL: http://www.hydrol-earth-syst-sci.net/16/4205/2012/, doi:10.5194/hess-16-4205-2012.

Chaussard, E., Bürgmann, R., Shirzaei, M., Fielding, E., Baker, B., 2014. Predictability of hydraulic head changes and characterization of aquifer-system and fault properties from insar-derived ground deformation. Journal of

Geophysical Research: Solid Earth 119, 6572–6590.
Chen, C.W., Zebker, H.A., 2001. Two-dimensional phase unwrapping with use of statistical models for cost functions in nonlinear optimization. JOSA A 18, 338–351.
Colesanti, C., Ferretti, A., Prati, C., Rocca, F., 2003. Monitoring landslides and tectonic motions with the permanent scatterers technique. Engineering geology 68, 3–14.
Colesanti, C., Wasowski, J., 2006. Investigating landslides with space-borne synthetic aperture radar (sar) interferometry. Engineering geology 88, 173–199.
Corsini, A., Borgatti, L., Caputo, G., De Simone, N., Sartini, G., Truffelli, G., 2006. Investigation and monitoring in support of the structural mitigation of large slow moving landslides: an example from ca'lita (northern apennines, reggio emilia, italy). Natural Hazards and Earth System Science 6, 55–61.
Cruden, D.M., Varnes, D.J., 1996. Landslides: investigation and mitigation. chapter 3-landslide types and processes. Transportation research board special report .
Fattahi, H., Amelung, F., 2015. Insar bias and uncertainty due to the systematic and stochastic tropospheric delay. Journal of Geophysical Research: Solid Earth 120, 8758–8773.
Ferretti, A., Fumagalli, A., Novali, F., Prati, C., Rocca, F., Rucci, A., 2011. A new algorithm for processing interferometric data-stacks: Squeesar. IEEE Transactions on Geoscience and Remote Sensing 49, 3460–3470.
Ferretti, A., Prati, C., Rocca, F., 2001. Permanent scatterers in sar interferometry. IEEE Transactions on geoscience and remote sensing 39, 8–20.
Fialko, Y., Sandwell, D., Simons, M., Rosen, P., 2005. Three-dimensional deformation caused by the bam, iran, earthquake and the origin of shallow slip deficit. Nature 435, 295–299. doi:10.1038/nature03425.
Fruneau, B., Achache, J., Delacourt, C., 1996. Observation and modelling of the saint-etienne-de-tinée landslide using sar interferometry. Tectonophysics 265, 181–190.
Goldstein, R.M., Werner, C.L., 1998. Radar interferogram filtering for geophysical applications. Geophysical research letters 25, 4035–4038.
Handwerger, A.L., Huang, M.H., Fielding, E.J., Booth, A.M., Bürgmann, R., 2019. A shift from drought to extreme rainfall drives a stable landslide to catastrophic failure. Scientific reports 9, 1569.
Handwerger, A.L., Roering, J.J., Schmidt, D.A., 2013. Controls on the seasonal deformation of slow-moving landslides. Earth and Planetary Science Letters 377, 239–247.
Handwerger, A.L., Roering, J.J., Schmidt, D.A., Rempel, A.W., 2015. Kinematics of earthflows in the northern california coast ranges using satellite interferometry. Geomorphology 246, 321–333.
Hilley, G.E., Bürgmann, R., Ferretti, A., Novali, F., Rocca, F., 2004. Dynamics of slow-moving landslides from permanent scatterer analysis. Science 304, 1952–1955.
Hooper, A., 2008. A multi-temporal insar method incorporating both persistent scatterer and small baseline approaches. Geophysical Research Letters 35.
Hooper, A., Segall, P., Zebker, H., 2007. Persistent scatterer interferometric synthetic aperture radar for crustal deformation analysis, with application to volcán alcedo, galápagos. Journal of Geophysical Research: Solid Earth 112.
Hooper, A., Zebker, H., Segall, P., Kampes, B., 2004. A new method for measuring deformation on volcanoes and

other natural terrains using insar persistent scatterers. Geophysical research letters 31.

Hooper, A., Zebker, H.A., 2007. Phase unwrapping in three dimensions with application to insar time series. JOSA A 24, 2737–2747.

Hu, B., Chen, J., Zhang, X., 2019. Monitoring the land subsidence area in a coastal urban area with insar and gnss. Sensors 19, 3181.

Intrieri, E., Raspini, F., Fumagalli, A., Lu, P., Del Conte, S., Farina, P., Allievi, J., Ferretti, A., Casagli, N., 2018. The maoxian landslide as seen from space: detecting precursors of failure with sentinel-1 data. Landslides 15, 123–133.

Malet, J.P., van Asch, T.W.J., van Beek, R., Maquaire, O., 2005. Forecasting the behaviour of complex landslides with a spatially distributed hydrological model. Natural Hazards and Earth System Sciences 5, 71–85. URL: http://www.nat-hazards-earth-syst-sci.net/5/71/2005/, doi:10.5194/nhess-5-71-2005.

Marroni, M., Treves, B., 1998. Hidden terranes in the northern apennines, italy: a record of late cretaceous-oligocene transpressional tectonics. The Journal of geology 106, 149–162.

Massonnet, D., Feigl, K.L., 1998. Radar interferometry and its application to changes in the earth's surface. Reviews of geophysics 36, 441–500.

Ni, W.J., Zhang, Z.Y., Sun, G.Q., Guo, Z.F., He, Y.T., 2014. The penetration depth derived from the synthesis of alos/palsar insar data and aster gdem for the mapping of forest biomass. Remote Sensing 6, 7303–7319. doi:10.3390/rs6087303.

Panini, F., Bettelli, G., Bonazzi, U., Gasperi, G., Fioroni, F., Fregni, P., 2002. Note illustrative alla Carta Geologica dItalia a scala 1:50.000. Foglio N. 237, Sasso Marconi.

Papani, G., De Nardo, M., Bettelli, G., Rio, D., Tellini, C., Vernia, L., Fornaciari, E., Iaccarino, S., Martelli, L., Papani, L., et al., 2002. Note illustrative della carta geologica ditalia alla scala 1:50.000, foglio 218, castelnuovo ne monti. EL. CA. Firenze, Servizio Geologico dItaliaRegione Emilia Romagna .

Patacca, E., Sartori, R., Scandone, P., 1993. Tyrrhenian basin and apennines. kinematic evolution and related dynamic constraints, in: Recent Evolution and Seismicity of the Mediterranean Region. Springer, pp. 161–171.

Picarelli, L., Urciuoli, G., Ramondini, M., Comegna, L., 2005. Main features of mudslides in tectonised highly fissured clay shales. Landslides 2, 15–30.

Prush, V., Lohman, R., 2014. Forest canopy heights in the pacific northwest based on insar phase discontinuities across short spatial scales. Remote Sensing 6, 3210–3226. doi:10.3390/rs6043210.

Raspini, F., Bianchini, S., Ciampalini, A., Del Soldato, M., Montalti, R., Solari, L., Tofani, V., Casagli, N., 2019. Persistent scatterers continuous streaming for landslide monitoring and mapping: the case of the tuscany region (italy). Landslides 16, 2033–2044. URL: https://doi.org/10.1007/s10346-019-01249-w, doi:10.1007/s10346-019-01249-w.

Servizio Geologico Sismico e dei Suoli della Regione Emilia-Romagna, R.E.R., 2019. Archivio storico delle frane della regione emilia-romagna. URL: http://geo.regione.emilia-romagna.it/schede/fs/fs_dis.jsp?id=60575.

Roering, J.J., Stimely, L.L., Mackey, B.H., Schmidt, D.A., 2009. Using dinsar, airborne lidar, and archival air photos to quantify landsliding and sediment transport. Geophysical Research Letters 36.

Rosen, P.A., Hensley, S., Joughin, I.R., Li, F.K., Madsen, S.N., Rodriguez, E., Goldstein, R.M., 2000. Synthetic aperture radar interferometry. Proceedings of the IEEE 88, 333–382.

Royden, L., Patacca, E., Scandone, P., 1987. Segmentation and configuration of subducted lithosphere in italy: An important control on thrust-belt and foredeep-basin evolution. Geology 15, 714–717.

Sandwell, D., Mellors, R., Tong, X., Wei, M., Wessel, P., 2011. Open radar interferometry software for mapping surface deformation. Eos, Transactions American Geophysical Union 92, 234–234.

Schlogel, R., Doubre, C., Malet, J.P., Masson, F., 2015. Landslide deformation monitoring with alos/palsar imagery: A d-insar geomorphological interpretation method. Geomorphology 231, 314–330. doi:10.1016/j.geomorph.2014.11.031.

Schmidt, D.A., Bürgmann, R., 2003. Time-dependent land uplift and subsidence in the santa clara valley, california, from a large interferometric synthetic aperture radar data set. Journal of Geophysical Research: Solid Earth 108.

Scoppettuolo, M., Cascini, L., Babilio, E., 2020. Typical displacement behaviours of slope movements. Landslides , 1–12.

Simoni, A., Ponza, A., Picotti, V., Berti, M., Dinelli, E., 2013. Earthflow sediment production and holocene sediment record in a large apennine catchment. Geomorphology 188, 42–53.

Tarayre, H., Massonnet, D., 1996. Atmospheric propagation heterogeneities revealed by ers-1 interferometry. Geophysical Research Letters 23, 989–992.

Tofani, V., Raspini, F., Catani, F., Casagli, N., 2013. Persistent scatterer interferometry (psi) technique for landslide characterization and monitoring. Remote Sensing 5, 1045–1065. doi:10.3390/rs5031045.

Wasowski, J., Bovenga, F., 2014. Investigating landslides and unstable slopes with satellite multi temporal interferometry: Current issues and future perspectives. Engineering Geology 174, 103–138.

Zebker, H.A., Rosen, P.A., Hensley, S., 1997. Atmospheric effects in interferometric synthetic aperture radar surface deformation and topographic maps. Journal of geophysical research: solid earth 102, 7547–7563.

Zebker, H.A., Villasenor, J., 1992. Decorrelation in interferometric radar echoes. IEEE Transactions on geoscience and remote sensing 30, 950–959.